

# Validation tests for GBS quantum computers using grouped count probabilities

Alexander S. Delliös, Margaret D. Reid, Bogdan Opanchuk and Peter D. Drummond  
*Centre for Quantum Science and Technology Theory,  
 Swinburne University of Technology, Melbourne 3122, Australia*

Computational validation is vital for all large-scale quantum computers. One needs computers that are both fast and also accurate. Here we apply precise, scalable, high order statistical tests to data from large Gaussian boson sampling (GBS) quantum computers. These tests can be used to validate the output results for such technologies, which are now claimed to demonstrate quantum supremacy. This method allows us to investigate the all-important issue of computational validity, rather than the more common question of speed. Such issues have not been investigated in detail before, as other methods were slow, or mostly restricted to the low-order correlations. Our very efficient, highly scalable general technique is also applicable to many other applications of quantum linear bosonic networks. We utilize positive-P phase-space simulations of grouped count probabilities (GCP) as a fingerprint for verifying the multimode data. This is exponentially more efficient for simulations than other phase-space methods, due to a much lower photo-count sampling error. One can randomly generate tests from an exponentially large menu of distinct very high-order grouped count tests. Each of these can be efficiently measured and simulated, providing a quantum verification method that is extremely difficult to replicate with a classical fake. Using these, we give a detailed comparison of theory with a recent 144-channel GBS experiment, including observable grouped correlations up to the largest order measured. Discrepancies of order  $100\sigma$  were observed from  $\chi^2$  validation tests, indicating systematic noise or other errors in current experiments that needs to be removed. We also show how one can disprove faked data, through the use of random high-order GCP tests from the resulting large test-suite.

## I. INTRODUCTION

Computers of all types require validation. This is a vital challenge with quantum computers which claim “quantum advantage”, as outputs may not be classically computable [1–5], making validation an exceptionally hard problem. A common difficulty with any computer is that there may be exponentially many inputs and outputs to test. If the outputs are random numbers, the distributions are usually exponentially sparse, which requires efficiently binning the data to check probabilities and conduct statistical testing [6].

Bosonic networks employed as quantum computers combine all three of these validation challenges, and are developing at an increasingly rapid pace. They promise to solve exponentially complex computational problems using room temperature optics, with a high degree of scalability and much simpler designs than computing architectures based on quantum logic-gates [7–9].

These networks include boson samplers, which utilize either nonclassical input number states [1, 10–16] or Gaussian squeezed states [2, 3, 17–20] to generate random, discrete counts by sampling matrix permanents [1, 21], Hafnians [2], or the Torontonian [3]. Which distribution is sampled depends on the type of input state and detectors used, although all are exponentially hard to directly compute at large sizes.

In this paper, we expand upon earlier work which showed how one can use grouped correlations to test outputs of Gaussian boson sampling (GBS) quantum computers with threshold detectors [22, 23]. This is achieved with scalable simulations using phase-space representations and continuous samples. These efficient techniques

allow one to compare theoretical and experimental output correlations and marginal probabilities. The simulations have identical moments and correlations to the ideal outputs. They have been scaled to very large sizes of up to 16,000 modes [22]. We compare our predictions with 144 mode experiments, and explain how our techniques can distinguish quantum data from classical fakes.

The GBS architecture is still in the domain of a few hundred modes, and treats non-computable random number generation. There are other, much larger bosonic networks in development. These are designed to solve hard optimization problems with up to 100,000 modes, [24–29], or generate large cluster states with up to a million modes [30]. Such larger systems have more practical applications. Despite this, the GBS case has great scientific interest. It has a simple enough architecture to allow a detailed theoretical model. By comparing theory with experiment, one can better understand how to validate network-based quantum computers, and how to test for experimental imperfections.

Successive large scale implementations of GBS quantum computers have claimed quantum supremacy [18–20]. Their growing size has rapidly outpaced previous classical verification methods, which either directly compute samples of output distributions such as the Torontonian, for small mode numbers [31, 32], or compute low order marginal probabilities at larger mode numbers [33, 34]. Neither has been able to verify all the measured high-order moments of the experimental data. Such traditional methods encounter severe barriers when computing the high-order correlations. The full distribution itself is known to be a #P-hard computational problem.

Phase-space methods are useful, although they do not

give photon counts directly. Doing this would be a #P-hard computational problem. The relevant algorithms have not yet been scaled even to the current experimental sizes, which are 100 times smaller. Despite this computational hardness, a testing protocol is essential to ensure that experimental errors such as drift, decoherence, and external noise are negligible. We can test this because our techniques are able to predict all the measurable statistical moments. Using these for validation can also be used to eliminate fakes, so as to prove that a classical imitation is significantly different.

Our methods can generate an exponentially large number of high-order tests. Clearly, these cannot all be implemented at once, which would take far too long. However, any attempt to fake the output counts will encounter a computationally hard “shell-game”. The counterfeiter cannot predict which test will be used. Thus, any classical algorithm designed just to deceive a small number of such tests is doomed. In all except an exponentially small number of scenarios, it will fail.

We use grouped photon count probabilities, binned in multiple dimensions. This gives an exponentially large number of tests. It therefore allows both a fine tuned comparison of experimental outputs with theory, and an exceptionally powerful method to differentiate between spoofed and experimental data. Comparisons are made with data from a 144-mode GBS experiment using threshold detectors, with measurements of up to 133-th order correlations [19]. We also consider a possible faking strategy with computable photon counts. These are generated from classical thermal states input into a linear network [35, 36].

Comparisons of marginal click correlation moment probabilities are also presented, as our numerical method allows one to efficiently generate comparisons for *all* possible correlation combinations. Click correlation moments are needed to compute cumulants, which are often used to compare the accuracy of samples from experiments that claim the presence of nontrivial high-order correlations [19], with low order marginal probability based classical algorithms [33].

An analysis of sampling errors generated from increased photon-number-resolving correlation order is given, as normally-ordered positive-P phase-space representations have no vacuum noise, and are often most efficient in simulating photo-detection. Due to its greatly reduced sampling errors, meaning that exponentially fewer samples are needed, we show that the positive-P method [37] is applicable to existing large-scale datasets, and is exponentially faster than proposed non-normally ordered methods [36, 38]. These, however, are very useful for analyzing multipartite entanglement, in which case the primary data generally comes from quadrature measurements [22].

Results of comparisons for all observables using  $\chi^2$  statistical tests demonstrate that the present 144-mode experimental dataset shows large deviations from the ideal GBS distribution, with deviations of order  $100\sigma$ . This

persists even when some decoherence is included in the squeezed inputs. Decoherence greatly improves agreement between theory and experiment, as observed by chi-square statistical tests [6, 39]. Yet the residual differences remain significant, and increase once high-order correlations are simulated using multi-dimensional GCPs.

The observed GBS differences are most likely due to nonlinearities, losses or further types of decoherence in the experiments. This leads to non-random behavior in samples, which is identified by computing the Z-statistic. However, experimental samples clearly show a better agreement with the expected distribution than fake data generated from input classical thermal states. It is an interesting open question in computer science whether all computable (ie, not exponentially slow) classical fakes can be identified using the powerful statistical tests that we have identified.

Our results highlight the importance of scalable validation methods for experimental data in current technologies. Scalability requirements and computability are fundamental to *any* theory that describes high-order multi-mode experiments. This includes Bose-Einstein condensates [40], dynamical phase-transitions [41], noisy quantum computers [42], random quantum circuits [43], multi-qubit photon-atom interactions [44], coherent Ising machines (CIM) [24, 29], and many others.

In summary, grouped count probabilities simulated in phase-space can validate the experimental outputs of large-scale gaussian boson sampling quantum technologies against quantum theoretical predictions, and distinguish them from classically faked data.

## II. PHASE-SPACE REPRESENTATIONS OF BOSONIC NETWORKS

To start with, we summarize background notation presented previously [22, 23] on representing the input and output states of a bosonic network with phase-space methods. Such representations are a natural fit for describing bosonic networks with Gaussian inputs. They are scalable and have analytical expressions which are simple to implement numerically. In some cases they are also applicable to other quantum technologies with nonlinearities and feedback, like the CIM [45, 46]. Choosing the correct representation to minimize computational sampling errors is of paramount importance. We show below why normally ordered positive-P method is the preferred choice for GBS, due to its scalability for high-order correlations compared to other methods.

### A. Input state

Linear networks are conceptually very simple. Without losses, the network itself is represented by a  $M \times M$  Haar random unitary matrix  $U$  [1, 2, 17, 47], however losses cause the network to become non-unitary. There-

fore, a lossy network is denoted by the  $M \times M$  transmission matrix  $\mathbf{T}$ . Out of  $M$  total input channels,  $N \subset M$  are filled with input states, which are then converted to  $M$  outputs via the linear network. In the case of GBS, these inputs are independent Gaussian single-mode squeezed states, which allow one to write the input state as  $\hat{\rho}^{(\text{in})} = \prod_j |\mathbf{r}\rangle \langle \mathbf{r}|$ , where  $\mathbf{r} = [r_1, \dots, r_N]$  is the squeezing vector.

Ideally, these inputs are pure squeezed states, which are nonclassical minimum uncertainty states defined entirely by their quadrature variances [48–50]. Following standard quantum optics techniques [51], these variances are defined as

$$\begin{aligned} \langle : (\Delta \hat{x}_j)^2 : \rangle &= 2(n_j + m_j) + 1 = e^{2r_j} \\ \langle : (\Delta \hat{y}_j)^2 : \rangle &= 2(n_j - m_j) + 1 = e^{-2r_j}, \end{aligned} \quad (2.1)$$

for normal ordering. Here,  $\hat{x}_j = \hat{a}_j + \hat{a}_j^\dagger$ ,  $\hat{y}_j = (\hat{a}_j - \hat{a}_j^\dagger)/i$  are the quadrature operators which obey the commutation relation  $[\hat{x}_j, \hat{y}_k] = 2i\delta_{jk}$  and allow one to write the requirement for a minimum uncertainty state as  $\langle : (\Delta \hat{x}_j)^2 : \rangle \langle : (\Delta \hat{y}_j)^2 : \rangle = 1$ . Meanwhile,  $n_j = \sinh(r_j)$  and  $m_j = \cosh(r_j) \sinh(r_j)$  are the input photon number and coherence per mode, respectively.

Experimentally generating pure squeezed states is challenging. Laboratory equipment such as lasers, polarizing beamsplitters, mirrors and phase-shifters will inevitably introduce decoherence due to laser noise, temporal drift, refractive index fluctuations [52], mode mismatch [18] and dephasing effects [53]. This means that the squeezed states can no longer be considered pure, such that  $\langle : (\Delta \hat{x}_j)^2 : \rangle \langle : (\Delta \hat{y}_j)^2 : \rangle > 1$ .

Therefore, to accurately model an experimental implementation of bosonic networks, one needs to account for this additional decoherence. We do this by using a model of thermal squeezed states [54], where a beamsplitter attenuates the input intensity by a factor of  $1 - \epsilon$  while adding  $n_j^{\text{th}} = \epsilon n(r_j)$  thermal photons per mode. This alters the input coherence as  $\tilde{m}_j = (1 - \epsilon)m(r_j)$ , whilst keeping the input photon number unchanged. The advantage of this model is that one can easily test a variety of input states from thermal,  $\epsilon = 1$ , to pure squeezed states,  $\epsilon = 0$ , and anything in between, by simply changing  $\epsilon$ .

## B. Phase-space representations of squeezed states

Nonclassical states such as squeezed states can be readily simulated using a variety of phase-space representations. However, for linear networks one is typically restricted by the type of detector used. If normally ordered photo-number-resolving (PNR) detectors are used, any non-normally ordered representation introduces vacuum

noise in the initial stochastic samples. We show below that this causes a rapid growth of computational sampling errors when computing high-order intensity correlations.

Although the normally ordered Glauber diagonal P-representation [55] at first may seem a good fit, it is singular for non-classical inputs such as squeezed states. However, for classical input states such as thermal states, the diagonal P-representation can be used to generate classical-like fake photon counts [35, 36].

To simulate the quantum inputs, we focus instead on the generalized P-representation [56], Wigner representation [57, 58] and Q-function [59] which all can give positive, non-singular distributions for squeezed state inputs.

### 1. Generalized P-representation

The normally ordered generalized P-representation produces a distribution in phase-space that is always exact and non-singular for any input quantum state. It is written in terms of the density matrix as

$$\hat{\rho} = \int \int P(\boldsymbol{\alpha}, \boldsymbol{\beta}) \hat{\Lambda}(\boldsymbol{\alpha}, \boldsymbol{\beta}) d\mu(\boldsymbol{\alpha}, \boldsymbol{\beta}), \quad (2.2)$$

where  $\hat{\rho}$  is expanded over a subspace of the complex plane,  $\boldsymbol{\alpha}, \boldsymbol{\beta}$  are independent coherent state amplitude vectors [60] and

$$\hat{\Lambda}(\boldsymbol{\alpha}, \boldsymbol{\beta}) = \frac{|\boldsymbol{\alpha}\rangle \langle \boldsymbol{\beta}^*|}{\langle \boldsymbol{\beta}^* | \boldsymbol{\alpha} \rangle} \quad (2.3)$$

is the off-diagonal coherent state projector.

The projection operator projects the density matrix onto multi-mode coherent states. This is responsible for the exact and non-singular nature of the generalized-P distribution for quantum inputs as it doubles the classical phase-space dimension, which allows off-diagonal coherent state amplitudes with  $\boldsymbol{\beta} \neq \boldsymbol{\alpha}^*$  to exist in the basis. These represent nonclassical quantum superposition states [56, 61].

The generalized P-representation is the name given to a family of normally ordered representations with different distributions  $P(\boldsymbol{\alpha}, \boldsymbol{\beta})$ , the form of which is dependent on the integration measure  $d\mu(\boldsymbol{\alpha}, \boldsymbol{\beta})$  [56]. Here, we focus on the positive P-representation which is obtained when  $d\mu(\boldsymbol{\alpha}, \boldsymbol{\beta}) = d^2\boldsymbol{\alpha} d^2\boldsymbol{\beta}$ , which is a  $4M$ -dimensional volume integral, and  $\boldsymbol{\alpha}, \boldsymbol{\beta}$  can vary along the whole complex plane. By taking the real part of Eq.(2.2), the density matrix becomes hermitian and can be sampled efficiently.

Because it gives an efficiently sampled, non-singular and strictly positive output distribution, the positive P-representation is ideal for simulating bosonic networks with squeezed state inputs due to its probabilistic properties combined with operator normal-ordering, which introduces a one-to-one relationship between operator moments and stochastic moments [37]:

$$\langle \hat{a}_{j_1}^\dagger, \dots, \hat{a}_{j_n} \rangle = \langle \beta_{j_1}, \dots, \alpha_{j_n} \rangle_P. \quad (2.4)$$

This relationship is valid for any generalized P-representation, where  $\langle \dots \rangle$  denotes a quantum expectation value and  $\langle \dots \rangle_P$  is a generalized-P stochastic average.

The input state density matrix  $\hat{\rho}^{(\text{in})}$  can be written in terms of the positive-P distribution by expanding each squeezed state  $|\mathbf{r}\rangle$  as a line integral over a real coherent state [23, 62]. This gives

$$\hat{\rho}^{(\text{in})} = \text{Re} \int \int P(\mathbf{x}, \bar{\mathbf{y}}) \hat{\Lambda}(\mathbf{x}, \bar{\mathbf{y}}) d\mathbf{x} d\bar{\mathbf{y}}. \quad (2.5)$$

Here

$$P(\mathbf{x}, \bar{\mathbf{y}}) = \prod_j C_j e^{-(x_j^2 + \bar{y}_j^2)(\gamma^{-1} + 1/2) + x_j \bar{y}_j} \quad (2.6)$$

is a positive-P distribution for an input pure squeezed state, which is a Gaussian distribution on a positive  $x-y$  plane, although other contours are possible. Here,  $x_j = \alpha_j + \beta_j$ ,  $\bar{y}_j = \alpha_j - \beta_j$  are real quadrature variables,  $C_j = (1 + \gamma_j)^{1/4} / \sqrt{\pi \gamma_j}$  is the normalization constant and  $\gamma_j = e^{2r_j} - 1$  allows us to write the quadrature variances in a simple form.

So far, we have assumed the squeezing orientation  $\langle :(\Delta \hat{x}_j)^2 : \rangle > 0$  and  $\langle :(\Delta \hat{y}_j)^2 : \rangle < 0$ , as it is for a pure squeezed state. However, if there is large added decoherence, one may have  $\langle :(\Delta \hat{y}_j)^2 : \rangle > 0$  and one must choose a contour where  $\bar{\mathbf{y}} = i\mathbf{y}$  is imaginary. In this situation of large added decoherence, one has rotated to a classical phase-space,  $\boldsymbol{\alpha}_c = [\boldsymbol{\alpha}, \boldsymbol{\alpha}^*]$  with  $\boldsymbol{\beta} = \boldsymbol{\alpha}^*$ . This automatically leads to a classical-like Glauber-Sudarshan P-representation, which is a special case or subset of the generalized P-representations.

## 2. Classical phase-space representations

The symmetrically ordered Wigner representation and anti-normally ordered Q-function are both defined on a classical phase-space and each have a positive distribution for Gaussian input states.

For any Gaussian state, the Wigner distribution can be written in the simple form [51, 63, 64]

$$W(\boldsymbol{\alpha}_c) = \frac{1}{\pi^{2N}} \int d^2 \mathbf{z} \text{Tr} \left\{ \hat{\rho} e^{i\mathbf{z} \cdot (\hat{\mathbf{a}} - \boldsymbol{\alpha}) + i\mathbf{z}^* \cdot (\hat{\mathbf{a}}^\dagger - \boldsymbol{\alpha}^*)} \right\}, \quad (2.7)$$

where  $\text{Tr}\{\dots\}$  is a trace and  $\mathbf{z}$  is a complex vector, while the Q-function is written in the standard form [59]:

$$Q(\boldsymbol{\alpha}_c) = \frac{1}{\pi^N} \langle \boldsymbol{\alpha} | \hat{\rho} | \boldsymbol{\alpha} \rangle. \quad (2.8)$$

These representations are simple to implement. They have been used previously to obtain analytical expressions for the probability of a specific GBS output pattern [2, 3, 17] and to determine the classical simulability of noisy GBS networks [35]. Although this may seem appealing compared to the generalized P-representation, both introduce vacuum noise in the initial stochastic samples when used to analyze linear networks with photon-number detectors. We show below that the additional vacuum noise causes a rapid increase in sampling errors, making the Wigner and Q representations unsuitable for scalable, practical applications to high-order correlations in large-scale bosonic networks using photon-number detectors.

These methods are useful in other areas of quantum optics, however. For example, the Wigner representation is ideally suited to analyze quadrature measurements of multipartite entanglement, which is a symmetrically ordered measurement obtained from homodyne detectors [65–67].

One can use the amount of vacuum noise added with each representation to define a corresponding operator ordering parameter  $\sigma$ , which is similar to  $s$ -ordering [68]. Here,  $\sigma = 0$  denotes normal ordering,  $\sigma = 1/2$  symmetric ordering and  $\sigma = 1$  anti-normal ordering. This scheme allows one to vary easily between representations, as can be seen by writing the Wigner and Q-function distributions as convolutions of the generalized P-representation [53], which in terms of quadrature variables is defined as:

$$P_\sigma(\mathbf{x}_c, \bar{\mathbf{y}}_c) = \frac{1}{(\pi\sigma)^N} \int P_0 e^{-((\mathbf{x}_c - \mathbf{x})^2 - (\bar{\mathbf{y}}_c - \bar{\mathbf{y}})^2)/4\sigma} d\mathbf{x} d\bar{\mathbf{y}}. \quad (2.9)$$

Here,  $P_\sigma(\mathbf{x}_c, \bar{\mathbf{y}}_c)$  is a  $\sigma$ -ordered representation distribution,  $\mathbf{x}_c = \boldsymbol{\alpha} + \boldsymbol{\alpha}^*$  and  $\bar{\mathbf{y}}_c = \boldsymbol{\alpha} - \boldsymbol{\alpha}^*$  are quadrature variables defined on a classical phase-space and  $P_0 = P(\mathbf{x}, \bar{\mathbf{y}})$  is a generalized-P distribution. The Wigner and Q distributions for a pure squeezed vacuum state can now be obtained by substituting the positive-P distribution Eq.(2.6) and integrating over  $\mathbf{x}, \bar{\mathbf{y}}$ .

Using this ordering scheme, one can extend the normal ordered equivalence between operator moments and stochastic moments to the  $\sigma$ -ordered relation:

$$\left\langle \left\{ \hat{a}_{j_1}^\dagger, \dots, \hat{a}_{j_n} \right\}_\sigma \right\rangle = \langle \alpha_{j_1}^*, \dots, \alpha_{j_n} \rangle_\sigma, \quad (2.10)$$

where  $\{\dots\}_\sigma$  and  $\langle \dots \rangle_\sigma$  denotes  $\sigma$ -ordered operator products and stochastic averages, respectively.

## C. Gaussian state inputs in $\sigma$ -ordered representations

Up to now, the phase-space distributions have assumed the input state is a product of independent pure squeezed



states which, as stated in subsection II A, does not fully represent experimental implementations of linear networks [22]. There are a number of experimental imperfections possible, from mode-mismatch to optical system drift, and even the possibility of nonlinearities, which are known to modify quantum noise [69].

To model such imperfections, the simulations include a beamsplitter model of decoherence which alters the quadrature variances to

$$\begin{aligned} \langle \{(\Delta \hat{x}_j)^2\}_\sigma \rangle &= (\Delta_{\sigma j}^x)^2 = 2(n_j + \sigma + \tilde{m}_j) \\ \langle \{(\Delta \hat{y}_j)^2\}_\sigma \rangle &= (\Delta_{\sigma j}^y)^2 = 2(n_j + \sigma - \tilde{m}_j), \end{aligned} \quad (2.11)$$

where we have also extended these equations to be valid for any  $\sigma$ -ordered measurement. It is likely that even more sophisticated models would be needed to fully explain the current experimental observations, but that is outside the scope of this paper.

Using Eq.(2.11), we can now construct initial stochastic samples, which are valid for any ordering, and are defined as [53]

$$\begin{aligned} \alpha_j &= (\Delta_{\sigma j}^x w_j + i \Delta_{\sigma j}^y w_{j+M})/2 \\ \beta_j &= (\Delta_{\sigma j}^x w_j - i \Delta_{\sigma j}^y w_{j+M})/2, \end{aligned} \quad (2.12)$$

where  $\langle w_j w_k \rangle = \delta_{jk}$  are real Gaussian noises.

#### D. Output density matrix

Practically, linear networks consist of a series of polarizing beamsplitters and mirrors, causing the  $N$  input modes to interfere, generating large amounts of entangled states, and converting the input state to the output state  $\hat{\rho}^{(\text{out})}$ .

In terms of phase-space distributions, this corresponds to transforming the initial stochastic amplitudes as  $\alpha' = T\alpha$  and  $\beta' = T^*\beta$ , which is valid for all representations. In the normally ordered case, the resulting output density matrix can therefore be sampled as before, but with a transformed projector:

$$\hat{\rho}^{(\text{out})} = \text{Re} \int \int P(\alpha, \beta) \hat{\Lambda}(T\alpha, T^*\beta) d\mu(\alpha, \beta). \quad (2.13)$$

To take into account losses and detector inefficiencies, one can include a larger unitary with loss channels, but only consider the sub-matrix of  $T$  for the channels that are measured. For example, in the matrix  $T = tU$ , all channels experience equal loss where  $t$  is an amplitude transmission coefficient. Due to the normal ordering property of the generalized P-representation, this method is also exactly equivalent to using a master equation method to treat losses.

Thermal noise or other random processes can also be included if present. For cases in which  $n^{th} > 0$  in the

loss reservoirs or  $\sigma > 0$  one must include these additional quantum and/or thermal noise terms with losses. Such noise terms correspond to  $\sigma$ -ordered noise in the reservoir modes. In the results given here, we assume that thermal noise only occurs in the input modes, and that the reservoirs are at zero temperature. When there are input thermal photons included with  $n^{th} \neq 0$ , the input distribution is no longer restricted to the real axis, but this causes no practical difficulties.

### III. GROUPED CORRELATION PROBABILITIES

Correlations provide a signature of measurable quantum states. For these to be a useful signature, they must be readily observable, relevant to interesting quantum features, and have a low enough sampling error to provide an unambiguous result. In this section, we review both Glauber intensity correlations and grouped count probabilities (GCP) of bosonic networks, which have already been successfully used to compare theory and experiment for an  $M = 100$  mode GBS experiment [22].

#### A. Intensity correlations

The most commonly used correlation in quantum optics is the  $n$ -th order Glauber intensity correlation [60]. In photonic experiments with PNR detectors [70–73], the expectation value of the product of normally ordered output number operators in a set of up to  $M$  output modes is observed:

$$G^{(n)}(c_j) = \langle : (\hat{n}'_j)^{c_j} \dots (\hat{n}'_M)^{c_M} : \rangle, \quad (3.1)$$

where  $\hat{n}'_j = \hat{a}_j^{\dagger(\text{out})} \hat{a}_j^{(\text{out})}$  is the output photon number operator, while  $c_j = 0, 1, 2, \dots$  is the number of photon counts at the  $j$ -th detector, and  $n = \sum c_j$  is the correlation order.

In the positive-P phase-space representation, output correlations are obtained by computing moments which, due to the equivalence of operator and stochastic moments, are obtained simply by replacing  $\hat{n}'_j$  with  $n'_j = \alpha'_j \beta'_j$ , such that for a large number of samples

$$G^{(n)} = \langle (n'_j)^{c_j} \dots (n'_M)^{c_M} \rangle_0. \quad (3.2)$$

In the  $\sigma$ -ordered phase-space case, the required re-ordering of all number operators produces a correction term which must be included to remove the vacuum noise introduced by each operator. Provided  $c_j = 0, 1$ , this correction allows the stochastic variable to become equivalent to the normally ordered output particle number, when  $T$  is unitary, via the replacement

$$n'_j = \alpha'_j \beta'_j - \sigma. \quad (3.3)$$

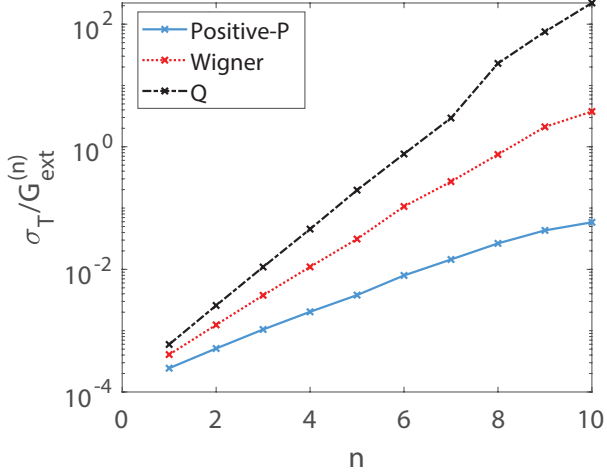


Figure 1. Comparison of sampling error growth for an  $M = 20$ ,  $N = 20$  GBS with uniform pure squeezed state inputs and  $E_S = 4.8 \times 10^7$  samples. The ratio of theoretical sampling errors,  $\sigma_T$ , with an exactly computed intensity correlation,  $G_{ext}^{(n)}$ , is plotted. Q-function simulations are denoted by the dashed black line, and add the largest amount of vacuum noise per photon number. The Wigner representation simulations are denoted by the red dotted line, which adds half a quantum of noise per photon number, whilst the positive-P representation adds no vacuum noise and corresponds to the solid blue line, with far lower sampling error. Details are given in Section (IV).

In principle,  $c_j$  is arbitrary and can be limited to  $c_j = 0, 1$  in some cases, but for more general cases with  $c_j > 1$  the non-normally-ordered expressions become cumbersome, and are not listed here.

This in itself may not be a severe limitation, as GBS proposals with PNR detectors often assume the probability of observing more than one photon at a detector to be small [2, 17]. However, as shown in Fig (1), the computational sampling error of Wigner and Q-function simulations grows rapidly with correlation order, making them unsuitable for generating moments to compare with experiment.

For cases with sufficiently low flux corresponding to small mean photon numbers, threshold detectors are equivalent to PNR detectors. The intensity correlation is also the probability of an  $N$ -fold coincidence count  $P_N$ . This allows one to write the correlation as a simple product of output number operators, such that

$$P_N \equiv \left\langle \prod_j \hat{n}_j' \right\rangle. \quad (3.4)$$

At high flux levels, a single PNR detector may register more than one count and the output is no longer binary. In such cases, we must distinguish between PNR and threshold detectors. To get accurate results for threshold detectors, a different operator is used.

## B. Grouped count correlations for saturating detectors

To date, multiple GBS experiments of large scale networks have been conducted using both PNR detectors [20], and threshold, or click, detectors which saturate for more than one count at a detector [18, 19]. When PNR detectors are used, one samples from the Hafnian distribution [2, 17], whilst threshold detectors are equivalent to sampling from the Torontonian distribution [3].

We focus on experiments using the latter detector type, with outputs being binary numbers where the  $j$ -th detector records  $c_j = 1$  for a photon detection event, or click, and  $c_j = 0$  for no detection event. Therefore, a network of  $M$  detectors will produce binary patterns represented by the count vector  $\mathbf{c}$ , with  $2^M$  possible patterns available. Each detector is defined by the normally-ordered projection operator [74]

$$\hat{\pi}_j(c_j) =: e^{-\hat{n}_j'} \left( e^{\hat{n}_j'} - 1 \right)^{c_j} :. \quad (3.5)$$

The expectation of this for  $c_j = 1$  is the first-order click correlation moment,  $\langle \hat{\pi}_j(1) \rangle$ , which is the probability of observing a click at the  $j$ -th detector. The projection operator for a specific binary pattern  $\mathbf{c}$  is  $\hat{\Pi}(\mathbf{c}) = \bigotimes_{j=1}^M \hat{\pi}_j(c_j)$ , whose expectation value is the Torontonian function [3]. This is exponentially small in almost all cases, which means it cannot be measured for large scale experiments due to experimental sampling errors.

To compute output probabilities of bosonic networks with threshold detectors *without* directly generating discrete patterns we use grouped count probabilities (GCP). These generate moments of multiple possible output patterns. They also allow one to carry out exponentially many high-order correlation tests.

A GCP computes the probability of observing  $\mathbf{m} = (m_1, \dots, m_d)$  grouped counts in  $d$ -dimensions. Each grouped count  $m_j$  is obtained by summing over all binary patterns. These are combined into bins based on the number of detector counts in a subset  $S_j$  of all  $M$  output modes, such that  $m_j = \sum_{i \in S_j} c_i$ . A  $d$ -dimensional GCP is therefore defined as [22]

$$\mathcal{G}_S^{(n)}(\mathbf{m}) = \left\langle \prod_{j=1}^d \left[ \sum_{\sum_{i \in S_j} c_i = m_j} \hat{\Pi}_{S_j}(\mathbf{c}) \right] \right\rangle, \quad (3.6)$$

where  $n = \sum_{j=1}^d M_j \leq M$  is the total click correlation order, following Glauber's definition [60], and  $\mathbf{S} = (S_1, S_2, \dots)$  is the vector of disjoint subsets of  $\mathbf{M} = (M_1, M_2, \dots)$  output modes. These includes marginal probabilities where some detectors are not monitored, as well as simple moments like the Torontonian. However, a GCP has the advantage of being both measurable and including data from all detectors if required.

As well as being unmeasurable, the Torontonian is not computable at large scale. There are no efficient direct techniques, and phase-space methods are only useful where the Torontonian has a large enough value to exceed the theoretical sampling error. However, many GCPs are both measurable and computable, as they are remarkably scalable using the positive-P representation. The normally ordered projection operator  $\hat{\pi}_j$  is computed via a simple replacement with the corresponding positive-P observable  $\pi_j$ , where output photon numbers  $n'_j$  are obtained from sampling the output distribution Eq.(2.13). The summation can then be efficiently carried out using a multi-dimensional inverse discrete Fourier transform with Fourier angle  $\theta_j = 2\pi/(M_j + 1)$ . This removes all patterns that don't contain  $\mathbf{m}$  grouped counts.

A detailed description of the computational methods and the developed algorithm can be found in Refs.[22, 23].

### 1. Multi-dimensional binning of grouped correlations

The experimentally reported total count probability [18, 19], which is the probability of observing  $m$  clicks in any pattern, is typically one of the first comparison tests experimental samples are subjected to. It allows one to quickly determine whether outputs are close to the expected distribution obtained using pure squeezed state inputs, typically called the 'ideal' or 'ground truth' distribution in the literature.

However, Villalonga et al [33] has shown that total count distributions can be easily spoofed by classical algorithms which sample from low-order marginal probabilities. The second and third-order samplers generate distributions that are closer to an approximated ideal distribution than an experiment with the largest mean number of clicks to date [19]. Therefore, comparison tests are needed which utilize the true high-order correlations generated by interfering squeezed photons in a linear network, to help differentiate experimental and classical sampling algorithm output distributions.

This is where grouped probabilities with dimension  $d > 1$  become particularly useful for statistical comparisons. A  $d > 1$ -dimensional grouped correlation of order  $n = M$  is the probability of observing  $m_1, \dots, m_d$  grouped counts in the subsets

$$\mathbf{S} = (S_1, \dots, S_d) = (\{1, \dots, M/d\}, \dots, \{M/d + 1, \dots, M\}), \quad (3.7)$$

such that  $m_1 = \sum_1^{M/d} c_1$ ,  $m_d = \sum_{M/d+1}^M c_{M/d+1}$ .

The first benefit of multi-dimensional GCPs is that the increased dimension leads to a large number of bins, or data points, that are available for statistical testing. When combined with the model of added decoherence described above, this produces a finely tuned comparison of experimental and theoretical outputs, allowing one to determine the accuracy of experimental samples. If additional discrepancies are present after simple decoherence

effects are included, this could indicate that further imperfections or nonlinearities are affecting the network.

The increased dimension also means higher-order correlations present in experimental data are more statistically significant. This is the main advantage of multi-dimensional GCPs simulated in phase-space, as it provides a powerful method of sifting out data that has been spoofed by classical algorithms which sample from low order correlations, since they will only contain correct correlations up to a specific order.

Additional tests can be performed by randomly permuting each binary pattern. This changes the output modes that are contained in each subset  $S_j$ , leading to different values of  $m_j$  for each permutation. Without repetitions, there are  $M!$  possible permutations of each pattern, giving  $M!/d$  possible ways of computing  $m_1, \dots, m_d$ . This produces exponentially many non-trivial, randomized high-order tests per dimension, thus allowing exponentially many comparisons to take place, with different high-order correlations being observed in each test.

If repeated comparisons show that differences between theoretical and experimental outputs remain statistically significant, one can hypothesize that experimental imperfections have caused samples to become inaccurate. These random permutation tests can be simulated efficiently by applying the same permutation used on the experimental samples to the rows of the transmission matrix used in the phase-space simulation.

Theoretically, one can bin counts up to the maximum dimension possible, of  $d = M$ . However, this is strongly restricted by the experimental sampling error which increases with dimension  $d$ , due to each bin containing progressively fewer photon counts.

### 2. High-order click correlations

Multiple classical algorithms have been proposed that aim to spoof boson sampling experiments by generating photon count samples that are closer to the ideal distribution than experimental samples [33–35, 75]. To do this, proposed algorithms sample from approximated low-order marginal probabilities. These are computed using either input classical states such as thermal, distinguishable and squashed states [18, 35, 75] or by computing distributions which have correct connected correlations, also known as cumulants, of the ideal distribution for orders  $n \leq 3$  [33].

In terms of the click projector Eq.(3.5), the first two cumulants are defined as [19, 33, 76]:

$$\begin{aligned} \kappa_1 &= \langle \hat{\pi}_j(1) \rangle \\ \kappa_2 &= \langle \hat{\pi}_j(1) \hat{\pi}_k(1) \rangle - \langle \hat{\pi}_j(1) \rangle \langle \hat{\pi}_k(1) \rangle, \end{aligned} \quad (3.8)$$

which are the mean click count rate and covariance, respectively.

The usefulness of marginal probabilities arises because they contain information on the interference properties of  $n$  photons whilst ignoring the other  $M - n$  outputs [77, 78]. This information is used by classical sampling algorithms to estimate the ideal GBS distribution for large mode numbers, without actually sampling from the full Torontonian distribution.

Comparisons of cumulants have also been used to claim nontrivial high-order correlations are present in experimental samples and are consistent with expected ideal outputs [19]. However, the number of observable correlations scales as  $\binom{M}{n}$  making a direct computation of all correlations for  $n > 2$  computationally demanding at large  $M$ , as the number of possible combinations increases exponentially.

Using GCPs in phase-space, one can efficiently compute click correlation moments, which contain information about lower order moments [76], for *all* possible combinations. When combined with statistical testing, this produces a way to directly test the accuracy of specific high-order correlations present in experimental data at any order. To illustrate the application of GCPs, the third-order click correlation is obtained by setting  $n = 3$ ,  $S = \{j, k, h\}$  and  $\mathbf{m} = 3$  where  $\mathcal{G}_{\{j,k,h\}}^{(3)}(3) = \langle \hat{\pi}_j(1) \hat{\pi}_k(1) \hat{\pi}_h(1) \rangle$  is the probability of observing clicks at detectors  $j, k, h$ .

#### IV. SAMPLING ERRORS AND STATISTICAL TESTS

Linear networks produce sampled outputs with highly random observed photon counts due to photon paths becoming highly entangled in the network [18]. Statistical testing is vital to not only determine the accuracy of experimental samples but also departures of randomness in the photon counts [79].

Therefore, useful comparison simulations for validation and testing purposes must be accurate. This requires an analysis of sampling errors as the theoretical sampling error is required to be comparable or smaller than experimental sampling errors. In this section, we use Glauber intensity correlations to demonstrate how sampling errors grow with correlation order, illustrating the importance of choosing the correct phase-space representation to simulate bosonic networks with normally ordered detectors. We also give an overview of the statistical tests used throughout this paper.

##### A. Phase-space sampling error

The computational process for simulating phase-space representations is, in general, the same for any representation. Firstly, samples  $\alpha, \beta$  are generated by randomly sampling the input distribution  $E_S$  times. For linear networks, the number of initial random samples generated scales proportional to  $NE_S$  with a normally ordered

method, or as  $ME_S$  with non-normally ordered methods due to the additional algebraic terms which arise from vacuum noise.

If one is interested in dynamical simulations, the samples are then propagated through time to solve a stochastic differential equation [69], the form of which changes depending on the representation, the system Hamiltonian of interest and whether losses are taken into account. However, we are only interested in sampling from the output distribution, which is obtained by transforming the input states as described above.

Regardless of how the initial samples are transformed, output observables are obtained in the form of a stochastic average over the entire ensemble of samples. Therefore, the computation of the product of  $E_S$  randomly sampled normally ordered output photon numbers  $((n'_j)^{c_j})^{(k)}$  is

$$\bar{G}^{(n)} = \frac{1}{E_S} \sum_k^{E_S} ((n'_j)^{c_j})^{(k)} \dots ((n'_M)^{c_M})^{(k)}, \quad (4.1)$$

where the superscript  $k$  denotes the label of a stochastic trajectory in the overall ensemble, and  $\bar{G}^{(n)}$  denotes the ensemble mean.

This is valid with all orderings if re-ordered to normal order, provided the appropriate corrections are applied, and there are no correlation terms with  $c_j > 1$ . For normal ordering the terms can be repeated, and the result is not restricted to the unitary case, since losses can be included. In other cases, losses require additional noise terms. The other orderings also introduce additional algebraic terms if there are terms with  $c_j > 1$ .

Stochastic averages are estimates of the actual theoretical probability obtained from a quantum expectation value of an observed operator. In the limit  $E_S \rightarrow \infty$ , ensemble means converge to the actual theoretical probability such that in the case of Eq.(4.1),  $\bar{G}^{(n)} = \lim_{E_S \rightarrow \infty} \bar{G}^{(n)}$ .

Practical implementations of phase-space ensemble averages typically split ensembles into two sub-ensembles, so that  $E_S = N_S N_R$  [73]. This has a computational advantage, allowing efficient vector and multi-core parallel computing, and reducing time requirements for large ensemble sizes. There is also a statistical benefit: the first sub-ensemble  $N_S$  is the number of samples of the initial state. For  $N_S \rightarrow \infty$ , this gives sample averages that are normally distributed via the central limit theorem.

The second sub-ensemble  $N_R$  is the number of times the computation is repeated. This is equivalent to sampling from a normal distribution  $N_R$  times [73]. Therefore, the actual computation of the stochastic average Eq.(4.1) proceeds as

$$\bar{G}^{(n)} = \frac{1}{N_R} \sum_{i=1}^{N_R} \left( \frac{1}{N_S} \sum_{h=1}^{N_S} ((n'_j)^{c_j})^{(h)} \dots ((n'_M)^{c_M})^{(h)} \right)_{(i)}, \quad (4.2)$$

where  $h, i$  are the number of samples of the first and second sub-ensembles, respectively.

The second sub-ensemble also generates a statistical estimate of the theoretical sampling error of the ensemble mean as  $\sigma_T = \sigma_t / \sqrt{N_R}$ , where the sub-ensemble variance is [80, 81]:

$$\sigma_t^2 = \frac{\sum_{i=1}^{N_R} \left( \bar{G}_{(i)}^{(n)} - \bar{G}^{(n)} \right)^2}{N_R - 1}, \quad (4.3)$$

where we define the sub-ensemble mean as the  $i$ -th sum over the simulated data:

$$\bar{G}_{(i)}^{(n)} = \left( \frac{1}{N_S} \sum_{h=1}^{N_S} ((n'_j)^{c_j})^{(h)} \dots ((n'_M)^{c_M})^{(h)} \right). \quad (4.4)$$

Thus, the theoretical standard deviation in the mean for  $\bar{G}^{(n)}$  is readily obtained from the simulated fluctuations in  $\bar{G}_{(i)}^{(n)}$ .

A computationally friendly definition of  $\sigma_t$  can be derived which doesn't require computing  $\bar{G}^{(n)}$  before performing the summation using the expansion  $\sum_{i=1}^{N_R} \left( \bar{G}_{(i)}^{(n)} - \bar{G}^{(n)} \right)^2 = \sum_{i=1}^{N_R} \left( \bar{G}_{(i)}^{(n)} \right)^2 - \left( \sum_{i=1}^{N_R} \bar{G}_{(i)}^{(n)} \right)^2 / N_R$  [81].

Therefore, when  $N_R \gg 1$ , the theoretical sampling error of the correlation of  $E_S$  randomly sampled output photon numbers is estimated using the computationally efficient form

$$\sigma_T = \sqrt{\frac{\sum_{i=1}^{N_R} \left( \left( \bar{G}_{(i)}^{(n)} \right)^2 \right) - \left( \sum_{i=1}^{N_R} \left( \bar{G}_{(i)}^{(n)} \right) \right)^2 / N_R}{N_R (N_R - 1)}}. \quad (4.5)$$

As with any sampling procedure, the sampling error can be reduced by increasing the total number of ensembles which corresponds to increasing either sub-ensemble. How large each sub-ensemble is made typically depends on the computer. Increasing  $N_S$  requires more memory and processing power, while the size of  $N_R$  depends on whether multi-core computing is possible. The more cores available the faster the computation runs, although larger  $N_S$  will always increase the computation time.

### 1. Numerical comparisons

Intensity correlations with increasing order are computed using the Wigner, Q and positive-P representations for an  $M = 20$  mode bosonic network with unit transmission matrix and  $N = 20$  input pure squeezed states with a uniform squeezing parameter of  $\mathbf{r} = [1, \dots, 1]$ . For a network of this type, the output intensity correlation can be computed exactly. Therefore, one can use the ratio of theoretical sampling errors, estimated by Eq.(4.5),

and exactly computed correlations with increasing order to determine how sampling errors of each representation grow with correlation order.

Comparisons are plotted in Fig.(1) for simulations with  $E_S = 4.8 \times 10^7$  ensembles. Predictably, the Q and Wigner representations produce sampling errors multiple orders of magnitude larger than positive-P simulations, and become approximately equal to the computed intensity correlations at orders  $n = 6$  and  $n = 8$ , respectively. By contrast, the positive-P sampling error always remains small, with growth due to increased order arising from sampling distributions with decreasing probabilities.

This shows the benefit of the normally-ordered approach, which gives exponentially lower error with increased quantum scale.

## B. Statistical tests

The main statistical test used to quantify differences between phase-space simulations of GCPs and experimental outputs is a standard chi-square test [82]. Chi-square tests are a powerful statistical test commonly used to determine whether observed probabilities obtained from independent samples correspond to the predicted distribution of the system being tested [6, 79].

Let  $N_E$  denote the number of independent experimental observations. These are classified into  $k$  classes denoting all the possible outcomes one can observe. Each class has a theoretical probability of  $P_i$  with  $i = 1, 2, \dots, k$ , where the expected number of observations of the  $i$ -th class is  $N_E P_i$ , whilst the actual number of observations from an experiment is  $x_i$ .

The standard chi-square statistic is defined as [6]:

$$\chi^2 = \sum_{i=1}^k \frac{(N_E P_i - x_i)^2}{N_E P_i}, \quad (4.6)$$

which can be rewritten in terms of the estimated experimental probability  $P_i^e = x_i / N_E$  and variance  $\sigma_i^2 = P_i / N_E$ .

In terms of GCPs, we define the grouped count of the  $i$ -th class as  $m_{j_i}$  with each class representing a detector count bin. Using the shorthand notation  $\mathcal{G}_i$  to denote the true theoretical GCP of the  $i$ -th class, the experimental GCP is obtained using  $\mathcal{G}_i^e = m_{j_i} / N_E$  for  $N_E$  experimental samples. Since both experimental and theoretical probabilities are obtained via sampling, a slightly modified version of Eq.(4.6) is required [22]:

$$\chi^2 = \sum_{i=1}^k \frac{(\bar{\mathcal{G}}_i - \mathcal{G}_i^e)^2}{\sigma_i^2}, \quad (4.7)$$

where  $\bar{\mathcal{G}}_i$  is the phase-space simulated ensemble mean with  $\mathcal{G}_i = \lim_{E_S \rightarrow \infty} \bar{\mathcal{G}}_i$  and  $\sigma_i^2 = \sigma_{T,i}^2 + \sigma_{E,i}^2$  is the sum of

theoretical and experimental sampling errors. This ensures that both the distribution variances are included. For an ideal case, this combination is the theoretical variance of the difference between probabilities  $\Delta_i = \bar{g}_i - \mathcal{G}_i^e$ , which is called the difference error.

Due to Poissonian fluctuations, experimental sampling errors are estimated as  $\sigma_{E,i} \approx \sqrt{\mathcal{G}_i/N_E}$ . This is only valid for click detectors, as squeezed vacuum states are generated as superpositions of even photon numbers with outputs  $c_j = 0, 2, 4, \dots$  for PNR detectors, so they do not have simple binary outputs [49, 83].

Although the output errors follow a chi-square distribution, the input probabilities in the  $\chi^2$  sum are required to be both Gaussian, or approximately Gaussian as is the usual case, and independent. Small count numbers per bin means the experimental probability of that bin can no longer be approximated as a Gaussian. Therefore, chi-square tests are only performed for  $k$  valid bins, which we define as  $m_{j_i} > 10$  [6, 79].

For such Gaussian probabilities obtained via sampling, output results are expected to satisfy  $\chi^2/k - 1 \approx 0$ . The exact value of  $\chi^2/k$  is then an important indicator that experimental distributions have acceptable errors. However, if either sampling error satisfies  $\sigma_{T,i}, \sigma_{E,i} \approx \Delta_i$  while  $\sigma_{T,i} \gg \sigma_{E,i}$  or  $\sigma_{E,i} \gg \sigma_{T,i}$ , this does not give a useful test. Such issues arise due to large experimental sampling errors that occur for multi-dimensional GCPs with too many bins containing too few photon counts per bin.

When  $k \rightarrow \infty$ , the chi-square distribution  $\chi^2 \rightarrow \mathcal{N}(\mu, \sigma^2)$  with mean  $\mu = k$  and variance  $\sigma^2 = 2k$ , via the central limit theorem [84, 85]. This convergence is slow due to the skewness of the chi-square distribution [85]. Fortunately, an accurate and fast convergence is achieved using the Wilson-Hilferty transformation [84], where the transformed observable  $(\chi^2/k)^{1/3} \rightarrow \mathcal{N}(\mu, \sigma^2)$  for  $k \geq 10$  with  $\mu = 1 - \sigma^2$  and  $\sigma^2 = 2/(9k)$  [84, 85].

If the chi-square distribution can be approximated as a Gaussian, we can then perform the Z-statistic, or Z-score, test which has the general definition  $Z = (X - \mu)/\sigma$  [79, 81], where  $X$  is the test statistic. The Z-statistic determines how many standard deviations a test statistic is from its normally distribution expected mean. It is used to determine the probability that an observed experimental result could occur due to random fluctuations.

In terms of the Wilson-Hilferty transformed chi-square statistic  $X = (\chi^2/k)^{1/3}$ , we define an approximate Z-statistic as:

$$Z = \frac{(\chi^2/k)^{1/3} - (1 - 2/(9k))}{\sqrt{2/(9k)}}, \quad (4.8)$$

where an output of  $Z > 6$  indicates the test statistic has an extremely small probability of being observed.

When used in conjunction with random permutations of binary patterns, the Z-statistic is a powerful statistical test. Repeated large  $\chi^2/k$  departures produce large

Z-statistics, indicating that systematic errors are present in the experimental data, thus causing repeated observations of output distribution samples with very small probabilities.

## V. COMPARISONS OF THEORY AND EXPERIMENT

In this section, we compare theoretical GCPs with experimental data from a 144-mode GBS linear network [19]. This experiment obtained data for two different laser waists,  $125\mu m$  and  $65\mu m$ , and varying laser power. The first waist contains data for two different powers and the second waist, five different powers. Squeezing parameters are 50-mode vectors of amplitude  $\mathbf{r}$ , one for each laser power tested, while the transmission matrices  $\mathbf{T}$  are of size  $50 \times 144$  with two matrices in total, one for each laser waist.

Test statistics for comparisons of GCPs and first-order click correlation moments for all data sets are given however, comparison plots are also only shown for data from laser waist  $65\mu m$  and power  $1.65W$ . This is due to both practicality and claims of computational supremacy for this data set, as the cost of computing the Torontonian and generating random outputs scales with the number of modes and hence detector clicks.

### A. Multi-dimensional GCPs

For completeness, we first present comparisons of the experimentally reported total counts, which is computed as a  $d = 1$  dimensional GCP. Results of statistical tests for simulations using pure squeezed state inputs are reported in Table. I for each available data set. Since linear networks do not change the Gaussian nature of the input state, the output state will be Gaussian and one expects  $\chi_c^2/k \approx 1$ , although this is clearly not the case with reported data as  $\chi_c^2/k \gg 1$  for all experimental samples.

Although data set  $65\mu m$ ,  $1.65W$  has the largest  $\chi_c^2/k$  output of  $\chi_c^2/k \approx 1.9 \times 10^3$  for  $k = 85$ , Z-statistical tests indicate data from all experiments are exponentially far from their expected normally distributed mean for pure squeezed state inputs.

Improved agreement is obtained when small amounts of decoherence is added to simulations as shown in Table. I, which contains chi-square and Z-statistic outputs for each data set with their corresponding fitting parameters. Samples obtained from an experiment using laser waist and power  $65\mu m$ ,  $0.15W$  are closest to the simulated distribution, as indicated by  $\chi_c^2/k \approx 1.2 \pm 0.3$  with  $k = 27$ , than any other experimental data set once input decoherence corresponding to  $\approx 2\%$  mode mismatches is included. Unlike the pure squeezed state comparisons, the Z-statistic shows sample detector counts are close to the expected mean, indicating detector counts are sufficiently random for what would be expected from input

Waist	Power	Pure squeezed inputs			$t$	$\epsilon$	Thermalized squeezed inputs		
		$\chi_c^2/k$	$k$	$Z_c$			$\chi_\epsilon^2/k$	$k$	$Z_\epsilon$
$125\mu m$	1.412W	218	53	78	0.9972	0.0354	$2 \pm 0.5$	52	$4 \pm 1.5$
	0.5W	143	31	50	1.000665	0.03925	$20 \pm 2$	31	$20 \pm 1$
$65\mu m$	1.65W	1861	85	221	1.0109	0.0428	$10 \pm 1$	84	$23 \pm 2$
	1W	215	74	91	1.0026	0.0354	$6 \pm 1$	73	$15 \pm 2$
	0.6W	171	57	72	0.9966	0.0288	$2.5 \pm 1$	57	$6 \pm 2$
	0.3W	193	40	64	0.9972	0.0202	$7 \pm 1$	40	$12 \pm 1$
	0.15W	151	28	49	0.9972	0.0208	$1.2 \pm 0.3$	27	$0.7 \pm 1$

Table I. Statistical test outputs for comparisons of total counts  $\mathcal{G}_{144}^{(144)}(m)$  for all data sets obtained from a 144-mode GBS experiment [19]. Chi-square and approximate Z-statistic tests are generated from comparisons with phase-space simulations of  $E_S = 1.2 \times 10^6$  ensembles with both pure squeezed state inputs, denoted by the subscript  $c$ , and added decoherence, where  $\epsilon$  represents the thermal component added to the input states. To account for measurement errors, we multiply  $T$  by the fitting parameter  $t$ . Chi-square errors account for variations between repeated stochastic simulations for the corresponding  $t, \epsilon$  values, whilst Z-statistic errors correspond to outputs within chi-square errors. Fitting parameters for each data set obtain approximately equal statistical test outputs for  $t, \epsilon = \pm 0.0005$ , with the exception of  $125\mu m, 0.5W$  which has a variation of  $t = \pm 0.000005$  and  $\epsilon = \pm 0.00005$ .

Waist	Power	two-dimensional GCP		four-dimensional GCP	
		$Z_\epsilon$	$k$	$Z_\epsilon$	$k$
$125\mu m$	1.412W	145	702	153	28855
	0.5W	115	285	209	6479
$65\mu m$	1.65W	185	1567	200	98682
	1W	68	1267	109	70826
	0.6W	32	815	66	33271
	0.3W	43	445	99	13605
	0.15W	40	240	111	4695

Table II. Summary of Z-statistic test outputs for comparisons of GCPs with dimensions  $d = 2$  and  $d = 4$  for all GBS experimental data sets obtained from Ref.[19]. Simulations are performed with  $E_S = 1.2 \times 10^6$  ensembles and contain the same amount of input decoherence used to obtain the minimized total counts  $\chi^2/k$  outputs for each data set (see Table. I for fitting parameters).

squeezed states with added decoherence.

This is not the case with most other data sets, where Z-statistic outputs remain large. This is particularly the case with samples corresponding to  $65\mu m, 1.65W$ , which required the largest amount of input decoherence, equating to  $\approx 4\%$  mode mismatch, to obtain a three-orders of magnitude improvement in  $\chi^2/k$  values compared to pure state inputs. However, despite this significant improvement, the Z-statistic shows the probability of obtaining such an output is very small, indicating possible systematic errors in experimental samples.

To gain further insight into the experimental data, we present comparisons of multi-dimensional GCPs with fitting parameters corresponding to those given in Ta-

ble. I for experimental samples of every tested laser waist and power. Due to the large number of valid bins, the Z-statistic is the most useful statistical test for multi-dimensional GCPs, as the increased number of data points produces Gaussian distributions with much smaller variances, meaning comparisons are required to pass a more stringent test. Therefore, Z-statistic outputs for multi-dimensional GCPs are presented in Table. II.

We start by analyzing comparisons of a  $d = 2$  dimensional GCP, which is plotted in Fig.(3). Interestingly, the Z-statistic increases for all data sets when compared to total count outputs. This is particularly noticable for data from  $65\mu m, 0.15W$ , which sees a forty-fold increase when compared to the total counts Z-statistic of  $Z_\epsilon \approx 0.7$  for  $k = 27$ .

Comparisons with simulations using pure squeezed state inputs also record increasingly large statistical test outputs, with data from  $65\mu m, 1.65W$  giving  $Z_c \approx 422$  for  $k = 1582$ . Although this is again improved upon by adding decoherence in the inputs, with  $Z_\epsilon \approx 185$  for 1567 valid bins containing more than 10 counts, it is still exponentially large. Statistical testing notes experimental samples from all tested laser waists and powers are even further away from the expected normally distributed mean when compared to total count statistical tests.

This increased difference between theory and experiment for growing dimension is reflected in Fig.(2), which plots the normalized difference between theory and experiment and is defined as [22]:

$$\frac{\Delta \mathcal{G}^{(M)}(m)}{\sigma_m} = \frac{\bar{\mathcal{G}} - \mathcal{G}^e}{\sigma_m}. \quad (5.1)$$

The normalized difference follows from Eq.(4.7), except  $\sigma_m$  only sums over theoretical and experimental variances of the compared  $m$  grouped counts.

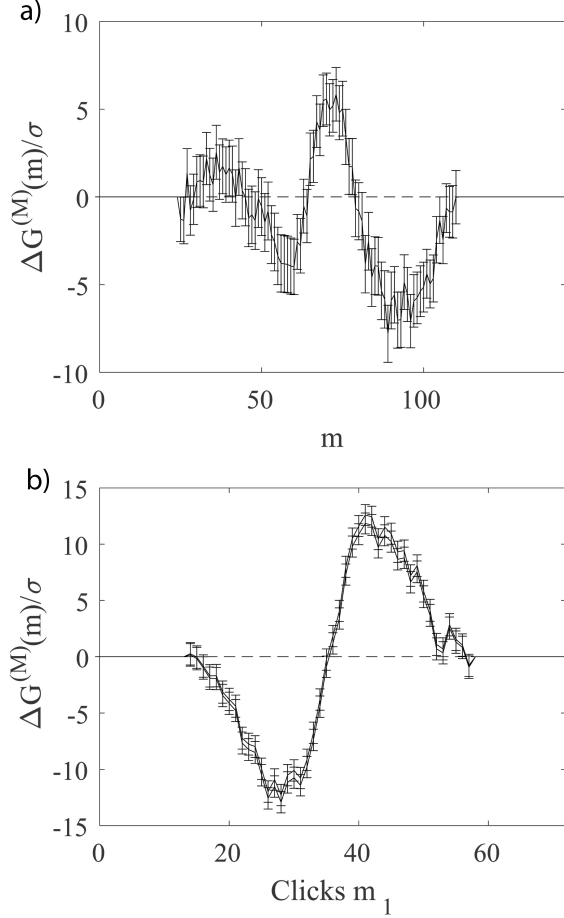


Figure 2. Normalized difference of experiment versus simulation for data set  $65\mu\text{m}$ ,  $1.65W$  with added decoherence. a) Plots results of  $\Delta G^{(M)}(m)/\sigma_m$  versus  $m$  for total count probability distributions. b) Results are  $\Delta G^{(M)}(m)/\sigma_m$  versus  $m_1$  of the one-dimensional slice shown in Fig.(3).b which is a  $d = 2$  dimensional GCP comparison. Upper and lower lines correspond to theoretical sampling errors.

Clearly, the finer tuned comparison obtained from increased dimensional GCPs shows experimental data has further, underlying differences that arise when higher-order correlations are simulated. To confirm this is the case, we can repeat the the  $d = 2$  dimensional GCP comparison tests an exponential number of times by randomly permuting each binary pattern. Although not all of these test can be performed, we randomly permute patterns from  $65\mu\text{m}$ ,  $1.65W$  and  $125\mu\text{m}$ ,  $1.412W$  to determine whether differences remain significant.

Since each random permutation obtains a different value for the grouped count  $m_j$ , comparison differences are likely to vary, with some tests showing better agreement than others. This is seen in Fig.(4) which compares the normalized difference of two random permutations, out of a tested ten, for samples from  $65\mu\text{m}$ ,  $1.65W$ . Although the average Z-statistic for all ten random permutations is  $\langle Z_\epsilon \rangle_{rp} \approx 115$  for  $\langle k \rangle_{rp} = 1568$ , where  $\langle \dots \rangle_{rp}$

denotes averages over random permutations, these two permutations obtain  $Z_\epsilon \approx 53$  with  $k = 1547$  and  $Z_\epsilon \approx 143$  for 1567 valid bins.

This decrease in statistical test outputs is also obtained from five different permutations of binary patterns from  $125\mu\text{m}$ ,  $1.412W$  with an average of  $\langle Z_\epsilon \rangle_{rp} \approx 94$  for  $\langle k \rangle_{rp} = 704$ . Despite the on average improved Z-statistic results for both types of experimental samples, each random permutation has consistently produced statistical outputs with exponentially small probabilities. Therefore, sample detector counts show likely departures from randomness for not only these data sets, but possibly all data sets from this experiment, when compared to both ideal and mode mismatched theoretical distributions.

To further verify experimental patterns are exhibiting possible non-randomness, we increased the dimension of the binning further to  $d = 4$  dimensions. Statistical testing outputs of each data set is given in Table. II and graphical comparisons of samples from  $65\mu\text{m}$ ,  $1.65W$  are shown in Fig.(5). This gives a dramatic increase in the number of data points containing more than 10 counts that can be used for testing.

At first glance, it appears as though the Z-statistic for some of the data sets has stabilized, particularly  $65\mu\text{m}$ ,  $1.65W$  and  $125\mu\text{m}$ ,  $1.412W$ , where the large increases seen when going from one to two-dimensions is not observed. This is further verified by performing comparisons for five random permutations of both data sets, giving averages of  $\langle Z_\epsilon \rangle_{rp} \approx 159$  for  $\langle k \rangle_{rp} = 99650$  and  $\langle Z_\epsilon \rangle_{rp} \approx 136$  for  $\langle k \rangle_{rp} = 29175$ , respectively.

However, a closer inspection shows experimental sampling errors for non-permutation comparisons of  $65\mu\text{m}$ ,  $1.65W$  have a mean value of  $\bar{\sigma}_E \approx 3.6 \times 10^{-7}$ . This is not only much larger than theoretical sampling errors,  $\bar{\sigma}_T \approx 2.1 \times 10^{-8}$ , but also reaches the level where  $\bar{\sigma}_E \approx \bar{\Delta}$ .

An analysis of sampling errors from  $125\mu\text{m}$ ,  $1.412W$  also shows  $\bar{\sigma}_T \gg \bar{\sigma}_E$  for non-permutation comparisons, where  $\bar{\sigma}_E \approx 5.4 \times 10^{-7}$  and  $\bar{\sigma}_T \approx 4.9 \times 10^{-8}$ . Therefore, experimental sampling errors are large enough that an artificially small  $\chi^2_\epsilon/k$  is obtained, causing the Z-statistic to appear to stabilize. Therefore, with currently available experimental data, experimental sampling errors become significant at four-dimensional GCP binning, rendering comparisons less accurate.

In other words, there is a balance required between test complexity and sample numbers. While more complex tests are much harder to fake because there are exponentially many of them, there is a price to pay. The amount of experimental data required to give low experimental sampling errors becomes unfeasibly large, reducing the power of the tests. Despite this limitation, we note that for the four-dimensional binning case,  $Z_\epsilon$  is still too large.

### 1. Classically generated photon counts

Classical states input into a linear bosonic network with normally ordered detectors generate an output state



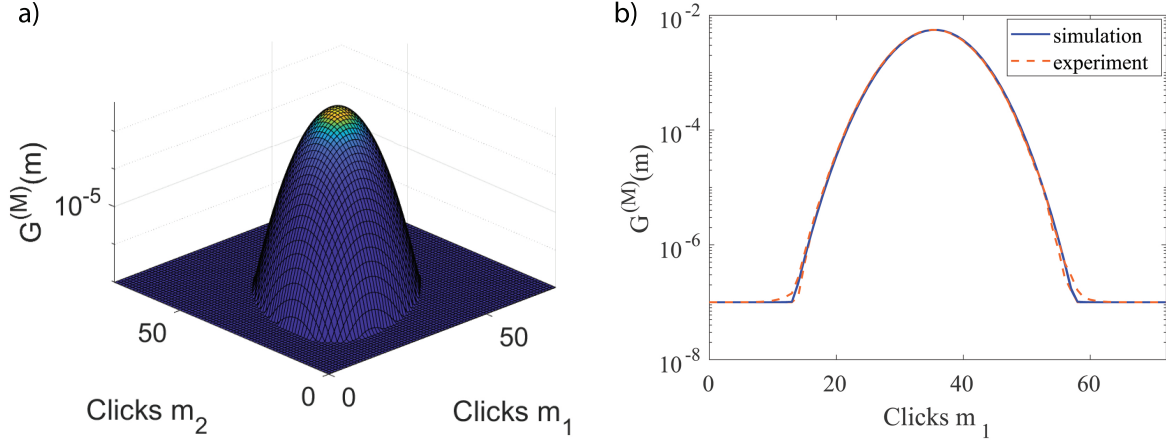


Figure 3. Comparisons of experimental data set  $65\mu m$ ,  $1.65W$  with simulations of  $1.2 \times 10^6$  stochastic ensembles for a  $d = 2$  dimensional GCP,  $\mathcal{G}_{72,72}^{(144)}(m_1, m_2)$ , with input decoherence. a) Full two-dimensional comparison distribution of GCPs with all  $72^2$  data points. b) One-dimensional slice through the maximum of the two-dimensional distribution. Plots a comparison of grouped count  $m_1$  where the solid blue line is the theoretical prediction and the orange dashed line is the experimental data.

whose distribution can be efficiently computed using Glauber's diagonal P-representation [35, 36], which is always positive for classical states such as thermal and coherent states [49, 83].

A variety of classical inputs have already been shown to poorly model experimental GBS data [18, 19, 33, 75]. However, to illustrate the usefulness of multi-dimensional GCPs in differentiating between faked and experimental data, we generate binary patterns using classical thermal states which are binned and compared to simulations of GCPs with pure squeezed state inputs. Squeezing parameters and transmission matrix corresponding a laser waist of  $65\mu m$  and power of  $1.65W$  are used for both simulations and generating fake patterns.

The diagonal P-representation is defined in terms of the density matrix [55]:

$$\hat{\rho} = \int P(\alpha_c) |\alpha_c\rangle \langle \alpha_c| d^2 \alpha_c, \quad (5.2)$$

which for the thermal state  $\hat{\rho}_{th} = (1 - \exp(-\hbar\omega/(k_B T))) \sum_n |n\rangle \langle n| \exp(-n\hbar\omega/(k_B T))$ , gives the diagonal-P distribution [76, 83]:

$$P(\alpha_c) = \frac{1}{\pi \langle \hat{n}_{th} \rangle} e^{-|\alpha|^2 / \langle \hat{n}_{th} \rangle}, \quad (5.3)$$

where  $\langle \hat{n}_{th} \rangle = 1/(\exp(-\hbar\omega/(k_B T)) - 1)$  is the thermal Bose distribution.

Using the method outlined in subsection IIC, input thermal samples are generated by letting  $\epsilon = 1$ . These are then transformed into outputs following  $\beta = T\alpha_c$  and  $\beta^* = (T\alpha_c)^*$ . We use Eq.(5.3) to formulate the first-order click correlation moment for thermal inputs as:

$$\langle \hat{\pi}_j(1) \rangle = 1 - e^{-|\beta_j|^2}, \quad (5.4)$$

where  $\langle \hat{\pi}_j(0) \rangle = e^{-|\beta_j|^2}$ .

Binary patterns are obtained by randomly sampling a Bernoulli distribution, where Eq.(5.4) is computed for  $E_S = 1 \times 10^6$  and used to generate  $5 \times 10^7$  binary patterns. Fake patterns are binned to generate GCPs following the method described above. Comparisons of total counts produce chi-square outputs of  $\chi_{th}^2/k \approx 8.52 \times 10^4$  for  $k = 61$  valid bins. This is an order of magnitude larger than total count comparisons of experimental samples.

When the dimension is increased to  $d = 2$ , comparisons of data generated from thermal state inputs produce a Z-statistic of  $Z_{th} \approx 1396$ , which is over three times larger than the corresponding Z-statistic from experimental samples. In the limit of large sample sizes, binned fake patterns will become approximately equal to low-order correlations, but the lack of correlations at higher-orders means the data is biased, leading to highly non-random behavior, since randomness arises from photon interference in a physical linear network.

## B. High-order click correlation moments

Click correlation moments have been used previously to compute cumulants to verify the presence of non-trivial, high-order correlations in experimental data and determine the accuracy of spoofing algorithms [19, 33]. Therefore, we present comparisons of correlation moments at various orders to discern whether specific experimental correlations agree with theoretical probabilities.

Statistical test results of comparisons for the simplest instance, the first-order moment  $\langle \hat{\pi}_j(1) \rangle$ , for all experimentally tested laser waists and powers are presented

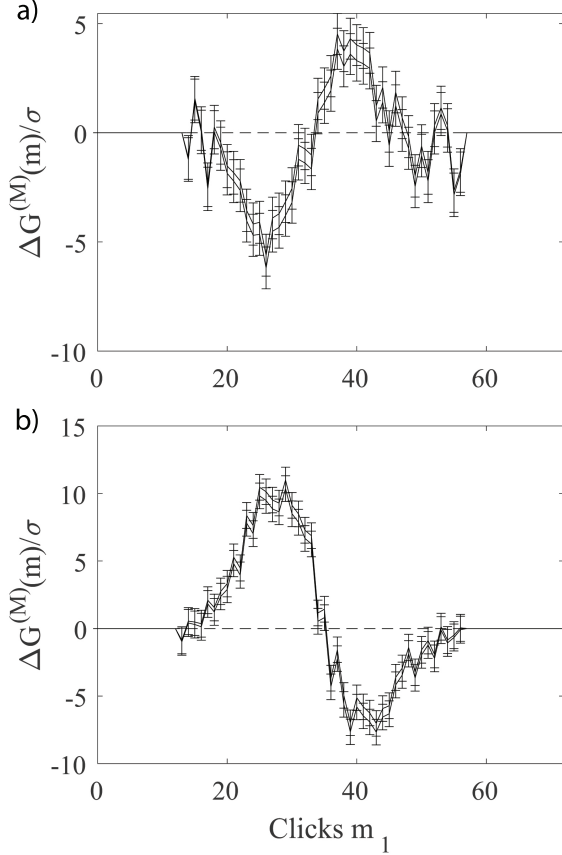


Figure 4. Comparison of normalized differences for two random permutations of binary patterns from data set  $65\mu m$ ,  $1.65W$ . The observable is a  $d = 2$  dimensional GCP with input decoherence which is simulated with  $E_S = 1.2 \times 10^6$ . Graphed results are of  $\Delta G^{(M)}(m)/\sigma_m$  versus  $m_1$ . a) Plots a random permutation test with a statistical test output of  $Z_\epsilon \approx 53$  with  $k = 1547$  valid bins, whilst b) plots a random permutation test with  $Z_\epsilon \approx 142$  for  $k = 1567$ . Upper and lower lines are  $\pm 1\sigma_{E,i}$  theoretical sampling errors.

	Waist	Power	$Z_c$	$Z_\epsilon$
$125\mu m$		$1.412W$	285	284
		$0.5W$	418	425
		$1.65W$	541	516
$65\mu m$		$1W$	405	397
		$0.6W$	267	263
		$0.3W$	235	231
		$0.15W$	198	196

Table III. Tabulated Z-statistic outputs for all 144 possible first-order click correlation moments of each data set. Simulations are performed using  $1.44 \times 10^7$  ensembles for input stochastic samples corresponding to pure squeezed states with  $\epsilon = 0$  and  $t = 1$ , denoted by the subscript  $c$ . Statistical test outputs with the subscript  $\epsilon$  denote simulations with small admixtures of thermal decoherence corresponding to mode mismatches.

in Table. III. In contrast to total counts or multi-dimensional GCPs, added decoherence does little to improve statistical test outputs. Although the exact reason for this is unclear, all data sets deviate significantly from theory.

Figure 6 plots the  $n = 1$  order click correlation for  $65\mu m$ ,  $1.65W$  with a small admixture of thermal decoherence included in the simulation inputs. Although comparison plots appear visually matching, graphed normalized differences tell a different story (see Fig. (6).b). This is reflected in statistical testing, where  $Z_\epsilon \approx 516$  and  $Z_c \approx 541$ . Clearly, outputs have an exponentially small probability of occurring, with samples showing significant departures from randomness. Faked thermal samples show an improved Z-statistic than both experimental tests with  $Z_{th} \approx 429$  for simulations with pure squeezed states.

This deviation only increases with correlation order as seen in comparisons of click correlation moments of orders  $n = 2, 3$ . Statistical testing is performed for all possible combinations of output modes for data from  $65\mu m$ ,  $1.65W$ , following  $\binom{M}{n} = M!/(n!(M-n)!)$ , but only a small sample of these combinations are plotted in Fig.(7), for order  $n = 2$ , and Fig.(8) with  $n = 3$ . This is simply due to graphical simplicity, as the number of possible combinations scales exponentially.

Again, theoretical and experimental distributions may generate visually similar outputs, however Z-statistic results of  $Z_\epsilon \approx 4.3 \times 10^3$  and  $Z_\epsilon \approx 2.7 \times 10^4$  for  $n = 2, 3$ , respectively tell a different story. Every increase in correlation order sees an order of magnitude increase in Z-statistic results, indicating experimentally generated binary patterns display behaviour even further away from random.

These results show the importance of conducting statistical testing using all available combinations of output modes. Only using a sample of possible correlations leads to a the expected normally distributed mean and variance of the Wilson-Hilferty transformed chi-square output to change, such that the tests become less rigorous.

This also highlights the need for a more detailed model of losses and decoherence to fully analyze currently available experimental data. Another potential issue is non-linearity, which would lead to effects like four-wave mixing, and possibly explain these departures.

## VI. SUMMARY

In summary, statistical tests are essential for the validation and performance analysis of any large-scale quantum technology. These can detect departures from randomness in experimental data, and show the presence of systematic errors. Error-free operation is a crucial requirement for any computer, including the present application of linear networks as quantum random number generators [18]. These tests allow one to determine the extent of decoherence present in experimental set-ups,

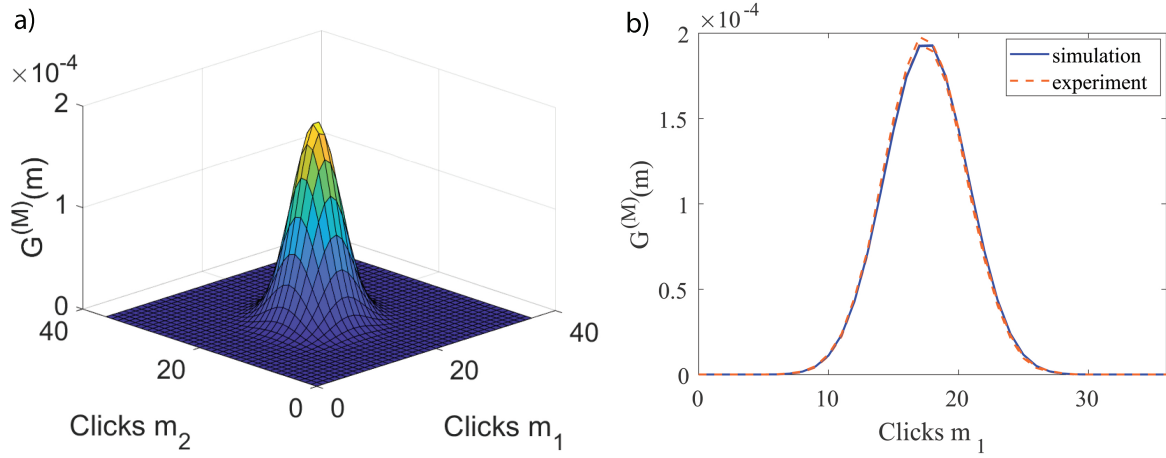


Figure 5. Comparisons of a  $d = 4$  dimensional GCP,  $\mathcal{G}_{36,36,36,36}^{(144)}(m_1, m_2, m_3, m_4)$ , for data set  $65\mu\text{m}$ ,  $1.65W$  containing  $N_E = 4 \times 10^7$  experimental binary patterns and phase-space simulations with  $E_S = 1.2 \times 10^6$  and added decoherence. a) A two-dimensional planar slice of grouped counts  $m_1, m_2$  of a four-dimensional distribution. All  $36^4$  data points are used for statistical tests. b) One-dimensional slice through the maximum of the two-dimensional planar slice. Plot is a comparison of  $m_1$ , where the solid blue line is the theoretical prediction and the orange dashed line is the experimental GCP.

which can cause experimental networks to become classically simulable [35]. The departures from ideal distributions also indicate possible errors in experimental set-ups which can lead to improved designs in future.

We have designed and implemented higher dimensional binning algorithms that allow the verification of boson-sampling quantum computers, with any one of exponentially many observable grouped probabilities being testable. Such methods combine a highly efficient positive-P phase-space method with a novel binning algorithm and a randomized test generator, giving a dynamic verification tool that can potentially prevent faking.

Our results demonstrate that the current generation of boson sampling quantum computers has outputs that significantly differ from ideal behavior when higher order correlations are taken into account. The cause of the experimental imperfections may include drift and noise

in parameter values, decoherence, and nonlinearity in the networks. Similar issues may also occur in other large scale quantum technologies, which are harder to model.

As a result, there is a clear need for the development of scalable phase-space simulators or other methods that can verify and benchmark the accuracy and performance of a wider range of large-scale quantum technologies.

## ACKNOWLEDGMENTS

This work was partly performed on the OzSTAR national facility at Swinburne University of Technology. OzSTAR is funded by Swinburne University of Technology and the National Collaborative Research Infrastructure Strategy (NCRIS). This research was funded through grants from NTT Phi Laboratories and the Australian Research Council Discovery Program.

- 
- [1] S. Aaronson and A. Arkhipov, *Theory of Computing* **9**, 143 (2013).
  - [2] C. S. Hamilton, R. Kruse, L. Sansoni, S. Barkhofen, C. Silberhorn, and I. Jex, *Phys. Rev. Lett.* **119**, 170501 (2017).
  - [3] N. Quesada, J. M. Arrazola, and N. Killoran, *Physical Review A* **98**, 062322 (2018).
  - [4] A. Bouland, *Nature Physics* **15**, 7 (2019).
  - [5] A. Deshpande, A. Mehta, T. Vincent, N. Quesada, M. Hinsche, M. Ioannou, L. Madsen, J. Lavoie, H. Qi, J. Eisert, D. Hangleiter, B. Fefferman, and I. Dhand, *Sci. Adv.* **8**, eabi7894 (2022).
  - [6] D. E. Knuth, *Art of computer programming, volume 2: Seminumerical algorithms* (Addison-Wesley Professional, 2014).
  - [7] F. Arute, K. Arya, R. Babbush, D. Bacon, J. C. Bardin, R. Barends, R. Biswas, S. Boixo, F. G. Brandao, D. A. Buell, *et al.*, *Nature* **574**, 505 (2019).
  - [8] Y. Wu, W.-S. Bao, S. Cao, F. Chen, M.-C. Chen, X. Chen, T.-H. Chung, H. Deng, Y. Du, D. Fan, M. Gong, C. Guo, C. Guo, S. Guo, L. Han, L. Hong, H.-L. Huang, Y.-H. Huo, L. Li, N. Li, S. Li, Y. Li, F. Liang, C. Lin, J. Lin, H. Qian, D. Qiao, H. Rong, H. Su, L. Sun, L. Wang, S. Wang, D. Wu, Y. Xu, K. Yan, W. Yang, Y. Yang, Y. Ye, J. Yin, C. Ying, J. Yu, C. Zha, C. Zhang, H. Zhang, K. Zhang, Y. Zhang, H. Zhao, Y. Zhao, L. Zhou, Q. Zhu, C.-Y. Lu, C.-Z. Peng, X. Zhu, and J.-W. Pan, *Phys. Rev. Lett.* **127**, 180501 (2021).
  - [9] M. Gong, S. Wang, C. Zha, M.-C. Chen, H.-L. Huang, Y. Wu, Q. Zhu, Y. Zhao, S. Li, S. Guo, H. Qian, Y. Ye,

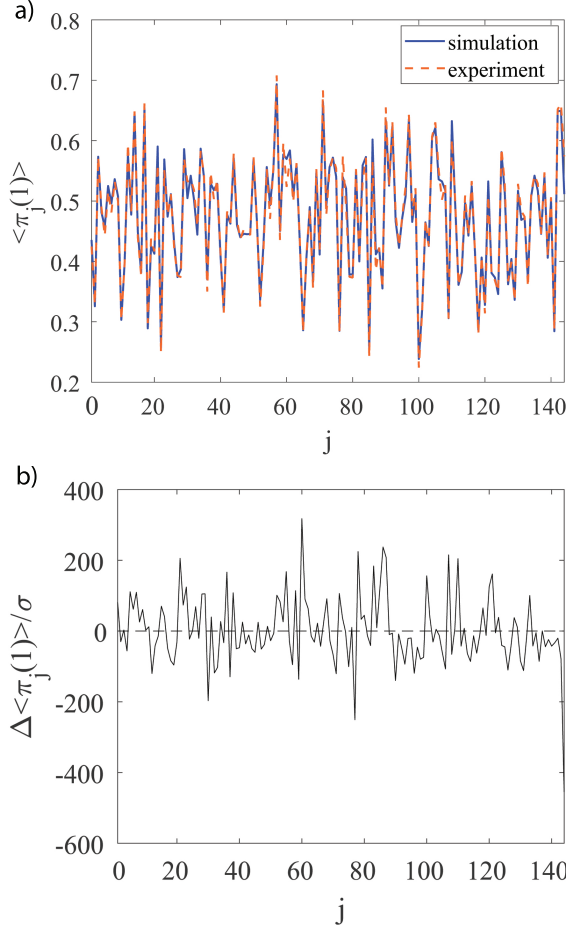


Figure 6. Comparison of theory versus experiment for all possible combinations of first-order count probabilities,  $\mathcal{G}_{\{j\}}^{(1)}(1) = \langle \hat{\pi}_j(1) \rangle$ , per channel  $j$ . Experimental samples are obtained from data set  $65\mu\text{m}$ ,  $1.65\text{W}$  whilst simulations are performed using  $E_S = 1.44 \times 10^7$  ensembles and a small admixture of thermal decoherence. a) Comparison plot with simulations represented by the solid blue and experimental distributions plotted with orange dashed lines. b) Normalized difference of  $\Delta \langle \hat{\pi}_j(1) \rangle / \sigma_m$  versus  $j$ .

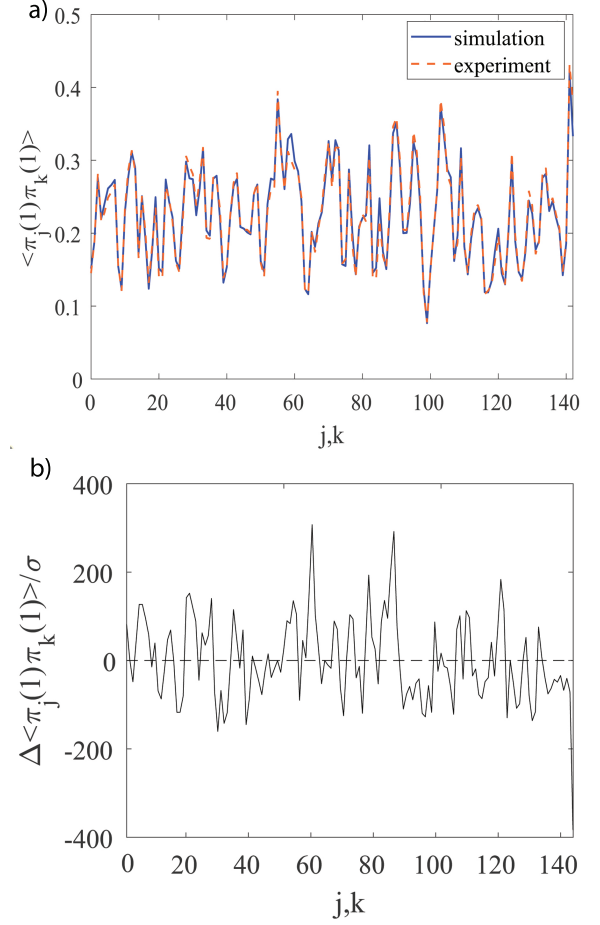


Figure 7. Theoretical and experimental comparison of a small sample of 143 out of a possible  $\binom{144}{2} = 10296$  second-order click correlation moments for modes  $j, k$ . Phase-space simulations use  $E_S = 1.44 \times 10^7$  ensembles whilst experimental samples are from  $65\mu\text{m}$ ,  $1.65\text{W}$ , with input decoherence corresponding to Table. I. a) Plotted comparisons of  $\mathcal{G}_{\{j,k\}}^{(2)}(2) = \langle \hat{\pi}_j(1) \hat{\pi}_k(1) \rangle$  versus channels  $j, k$  where simulations are represented by the solid blue and experimental outputs are plotted with orange dashed lines. b) Normalized difference of  $\Delta \langle \hat{\pi}_j(1) \hat{\pi}_k(1) \rangle / \sigma_m$  versus  $j, k$ .

- F. Chen, C. Ying, J. Yu, D. Fan, D. Wu, H. Su, H. Deng, H. Rong, K. Zhang, S. Cao, J. Lin, Y. Xu, L. Sun, C. Guo, N. Li, F. Liang, V. M. Bastidas, K. Nemoto, W. J. Munro, Y.-H. Huo, C.-Y. Lu, C.-Z. Peng, X. Zhu, and J.-W. Pan, *Science* **372**, 948 (2021).
- [10] M. A. Broome, A. Fedrizzi, S. Rahimi-Keshari, J. Dove, S. Aaronson, T. C. Ralph, and A. G. White, *Science* **339**, 794 (2013).
- [11] A. Crespi, R. Osellame, R. Ramponi, D. J. Brod, E. F. Galvao, N. Spagnolo, C. Vitelli, E. Maiorino, P. Mataloni, and F. Sciarrino, *Nature photonics* **7**, 545 (2013).
- [12] M. Tillmann, B. Dakić, R. Heilmann, S. Nolte, A. Szameit, and P. Walther, *Nature photonics* **7**, 540 (2013).
- [13] J. B. Spring, B. J. Metcalf, P. C. Humphreys, W. S. Kolthammer, X.-M. Jin, M. Barbieri, A. Datta, N. Thomas-Peter, N. K. Langford, D. Kundys, J. C. Gates, B. J. Smith, P. G. R. Smith, and I. A. Walmsley, *Science* **339**, 798 (2013).
- [14] N. Spagnolo, C. Vitelli, M. Bentivegna, D. J. Brod, A. Crespi, F. Flamini, S. Giacomini, G. Milani, R. Ramponi, P. Mataloni, *et al.*, *Nature Photonics* **8**, 615 (2014).
- [15] A. Crespi, R. Osellame, R. Ramponi, M. Bentivegna, F. Flamini, N. Spagnolo, N. Viggianiello, L. Innocenti, P. Mataloni, and F. Sciarrino, *Nature communications* **7**, 1 (2016).
- [16] H. Wang, J. Qin, X. Ding, M. C. Chen, S. Chen, X. You, Y. M. He, X. Jiang, L. You, Z. Wang, C. Schneider, J. J. Renema, S. Höfling, C.-Y. Lu, and J. W. Pan, *Physical Review Letters* **123**, 250503 (2019).
- [17] R. Kruse, C. S. Hamilton, L. Sansoni, S. Barkhofen, C. Silberhorn, and I. Jex, *Physical Review A* **100**, 032326 (2019).
- [18] H.-S. Zhong, H. Wang, Y.-H. Deng, M.-C. Chen, L.-C.



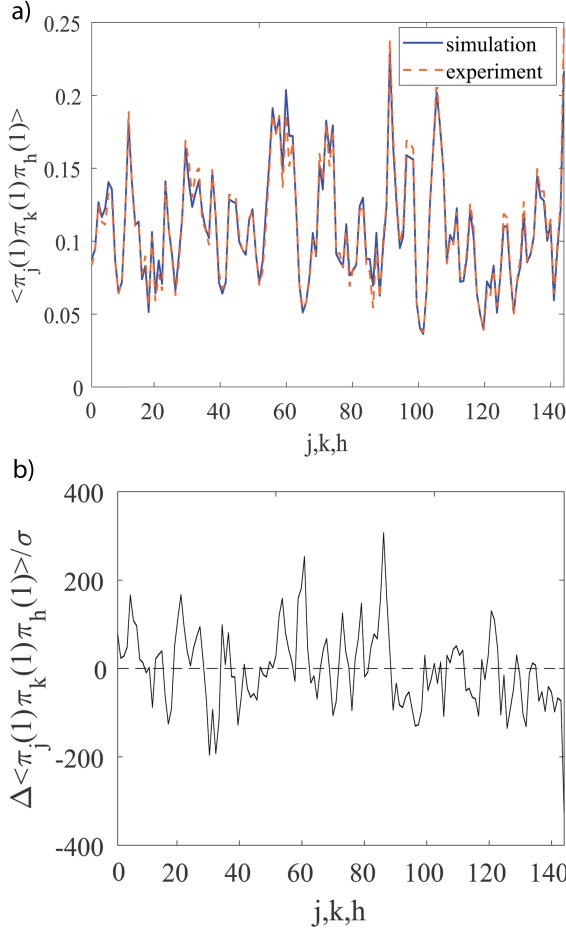


Figure 8. Errors in comparisons of theory and experiment for a subset of 142 third-order click correlations,  $\mathcal{G}_{\{j,k,h\}}^{(3)} = \langle \hat{\pi}_j(1)\hat{\pi}_k(1)\hat{\pi}_h(1) \rangle$ , versus modes  $j, k, h$ . Statistical tests are performed using all  $\binom{144}{3} = 487344$  possible combinations of output modes. a) Graphical comparisons with simulations denoted by the solid blue and obtained using  $E_S = 1.44 \times 10^7$  ensembles with added decoherence in the input stochastic samples, whilst the orange dashed lines denotes experimental outputs from data set  $65\mu\text{m}, 1.65W$ . b) Normalized difference of  $\Delta \langle \hat{\pi}_j(1)\hat{\pi}_k(1)\hat{\pi}_h(1) \rangle / \sigma_m$  versus  $j, k, h$ .

Peng, Y.-H. Luo, J. Qin, D. Wu, X. Ding, Y. Hu, *et al.*, Science **370**, 1460 (2020).

- [19] H.-S. Zhong, Y.-H. Deng, J. Qin, H. Wang, M.-C. Chen, L.-C. Peng, Y.-H. Luo, D. Wu, S.-Q. Gong, H. Su, Y. Hu, P. Hu, X.-Y. Yang, W.-J. Zhang, H. Li, Y. Li, X. Jiang, L. Gan, G. Yang, L. You, Z. Wang, L. Li, N.-L. Liu, J. J. Renema, C.-Y. Lu, and J.-W. Pan, Phys. Rev. Lett. **127**, 180502 (2021).
- [20] L. S. Madsen, F. Laudenbach, M. F. Askarani, F. Rortais, T. Vincent, J. F. F. Bulmer, F. M. Miatto, L. Neuhaus, L. G. Helt, M. J. Collins, A. E. Lita, T. Gerrits, S. W. Nam, V. D. Vaidya, M. Menotti, I. Dhand, Z. Vernon, N. Quesada, and J. Lavoie, Nature **606**, 75 (2022).
- [21] S. Aaronson, Proceedings of the Royal Society of London A: Mathematical, Physical and Engineering Sciences **467**, 3393 (2011).

- [22] P. D. Drummond, B. Opanchuk, A. Delliios, and M. D. Reid, Phys. Rev. A **105**, 012427 (2022).
- [23] A. Delliios, P. D. Drummond, B. Opanchuk, R. Y. Teh, and M. D. Reid (2021).
- [24] T. Shoji, K. Aihara, and Y. Yamamoto, Physical Review A **96**, 053833 (2017).
- [25] Z. Wang, A. Marandi, K. Wen, R. L. Byer, and Y. Yamamoto, Physical Review A **88**, 063853 (2013).
- [26] Y. Yamamoto, K. Aihara, T. Leleu, K.-i. Kawarabayashi, S. Kako, M. Fejer, K. Inoue, and H. Takesue, npj Quantum Information **3**, 1 (2017).
- [27] P. L. McMahon, A. Marandi, Y. Haribara, R. Hamerly, C. Langrock, S. Tamate, T. Inagaki, H. Takesue, S. Utsunomiya, K. Aihara, R. L. Byer, M. M. Fejer, H. Mabuchi, and Y. Yamamoto, Science **354**, 614 (2016).
- [28] A. Yamamura, K. Aihara, and Y. Yamamoto, Physical Review A **96**, 053834 (2017).
- [29] T. Honjo, T. Sonobe, K. Inaba, T. Inagaki, T. Ikuta, Y. Yamada, T. Kazama, K. Enbutsu, T. Umeki, R. Kasahara, K. ichi Kwarabayashi, and H. Takesue, Science Advances **7**, eabh0952 (2021), <https://www.science.org/doi/pdf/10.1126/sciadv.abh0952>.
- [30] J.-i. Yoshikawa, S. Yokoyama, T. Kaji, C. Sornphiphatphong, Y. Shiozawa, K. Makino, and A. Furusawa, APL Photonics **1**, 060801 (2016).
- [31] J. F. F. Bulmer, B. A. Bell, R. S. Chadwick, A. E. Jones, D. Moise, A. Rigazzi, J. Thorbecke, U.-U. Haus, T. Van Vaerenbergh, R. B. Patel, I. A. Walmsley, and A. Laing, Sci. Adv. **8**, eabl9236 (2022).
- [32] N. Quesada, R. S. Chadwick, B. A. Bell, J. M. Arrazola, T. Vincent, H. Qi, and R. García-Patrón, PRX Quantum **3**, 010306 (2022).
- [33] B. Villalonga, M. Y. Niu, L. Li, H. Neven, J. C. Platt, V. N. Smelyanskiy, and S. Boixo, arXiv preprint arXiv:2109.11525 (2021).
- [34] C. Oh, L. Jiang, and B. Fefferman, Spoofing cross entropy measure in boson sampling (2022), arXiv:2210.15021 [quant-ph].
- [35] H. Qi, D. J. Brod, N. Quesada, and R. García-Patrón, Physical review letters **124**, 100502 (2020).
- [36] S. Rahimi-Keshari, T. C. Ralph, and C. M. Caves, Phys. Rev. X **6**, 021039 (2016).
- [37] P. D. Drummond and C. W. Gardiner, J. Phys. A **13**, 2353 (1980).
- [38] S. Rahimi-Keshari, S. Baghbanzadeh, and C. M. Caves, Phys. Rev. A **101**, 043809 (2020).
- [39] K. Pearson, Biometrika **8**, 250 (1911).
- [40] T. Schweigler, V. Kasper, S. Erne, I. Mazets, B. Rauer, F. Cataldini, T. Langen, T. Gasenzer, J. Berges, and J. Schmiedmayer, Nature **545**, 323 (2017).
- [41] J. Marino, M. Eckstein, M. S. Foster, and A. M. Rey, Reports on Progress in Physics **85**, 116001 (2022).
- [42] R. Blume-Kohout, M. P. da Silva, E. Nielsen, T. Proctor, K. Rudinger, M. Sarovar, and K. Young, PRX Quantum **3**, 020335 (2022).
- [43] Y. Takeuchi and T. Morimae, Physical Review X **8**, 021060 (2018).
- [44] A. Z. Goldberg, A. M. Steinberg, and K. Heshami, arXiv preprint arXiv:2210.12167 (2022).
- [45] S. Kiesewetter and P. D. Drummond, Optics Letters **47**, 649 (2022).
- [46] S. Kiesewetter and P. D. Drummond, Phys. Rev. A **106**, 022409 (2022).
- [47] D. Hangleiter and J. Eisert, Computational advantage

- of quantum random sampling (2022), arXiv:2206.04079 [cond-mat, physics:quant-ph].
- [48] H. P. Yuen, Physical Review A **13**, 2226 (1976).
  - [49] P. D. Drummond and Z. Ficek, eds., *Quantum Squeezing* (Springer-Verlag, Berlin, Heidelberg, New York, 2004).
  - [50] H. Vahlbruch, M. Mehmet, K. Danzmann, and R. Schnabel, Physical Review Letters **117**, 110801 (2016).
  - [51] P. D. Drummond and M. Hillery, *The quantum theory of nonlinear optics* (Cambridge University Press, 2014).
  - [52] S. H. Perlmutter, M. D. Levenson, R. M. Shelby, and M. B. Weissman, Phys. Rev. B **42**, 5294 (1990).
  - [53] P. D. Drummond and B. Opanchuk, Physical Review Research **2**, 033304 (2020).
  - [54] H. Fearn and M. Collett, Journal of Modern Optics **35**, 553 (1988).
  - [55] R. J. Glauber, Phys. Rev. **131**, 2766 (1963).
  - [56] P. D. Drummond and C. W. Gardiner, Journal of Physics A: Mathematical and General **13**, 2353 (1980).
  - [57] E. Wigner, Phys. Rev. **40**, 749 (1932).
  - [58] J. E. Moyal, Mathematical Proceedings of the Cambridge Philosophical Society **45**, 99 (1949).
  - [59] K. Husimi, Proc. Phys. Math. Soc. Jpn. **22**, 264 (1940).
  - [60] R. J. Glauber, Phys. Rev. **130**, 2529 (1963).
  - [61] P. D. Drummond and S. Chaturvedi, Physica Scripta **91**, 073007 (2016).
  - [62] J. Janszky and A. V. Vinogradov, Physical review letters **64**, 2771 (1990).
  - [63] W. H. Louisell, *Quantum statistical properties of radiation* (Wiley, New York, 1973).
  - [64] M. Hillery, R. F. O'Connell, M. O. Scully, and E. P. Wigner, Phys. Rep. **106**, 121 (1984).
  - [65] P. van Loock and A. Furusawa, Physical Review A **67**, 052315 (2003).
  - [66] J. Sperling and W. Vogel, Physical review letters **111**, 110503 (2013).
  - [67] R. Y. Teh and M. D. Reid, Physical Review A **90**, 062337 (2014).
  - [68] K. E. Cahill and R. J. Glauber, Phys. Rev. **177**, 1857 (1969).
  - [69] S. J. Carter, P. D. Drummond, M. D. Reid, and R. M. Shelby, Physical Review Letters **58**, 1841 (1987).
  - [70] M. C. Tichy, K. Mayer, A. Buchleitner, and K. Mølmer, Phys. Rev. Lett. **113**, 020502 (2014).
  - [71] K. Mayer, M. C. Tichy, F. Mintert, T. Konrad, and A. Buchleitner, Phys. Rev. A **83**, 062307 (2011).
  - [72] M. Walschaers *et al.*, New Journal of Physics **18**, 032001 (2016).
  - [73] B. Opanchuk, L. Rosales-Zárate, M. D. Reid, and P. D. Drummond, Physical Review A **97**, 042304 (2018).
  - [74] J. Sperling, W. Vogel, and G. S. Agarwal, Phys. Rev. A **85**, 023820 (2012).
  - [75] J. Martínez-Cifuentes, K. M. Fonseca-Romero, and N. Quesada, Classical models are a better explanation of the Jiuzhang Gaussian Boson Samplers than their targeted squeezed light models (2022), arXiv:2207.10058 [quant-ph].
  - [76] C. Gardiner and P. Zoller, *Quantum Noise: A Handbook of Markovian and Non-Markovian Quantum Stochastic Methods with Applications to Quantum Optics*, Springer Series in Synergetics (Springer, 2004).
  - [77] J. J. Renema, arXiv:2012.14917 [quant-ph] (2020), arXiv:2012.14917 [quant-ph].
  - [78] J. J. Renema, Phys. Rev. A **101**, 063840 (2020).
  - [79] A. L. Rukhin, J. Soto, J. R. Nechvatal, M. E. Smid, E. B. Barker, S. D. Leigh, M. Levenson, M. Vangel, D. L. Banks, *et al.*, A statistical test suite for random and pseudorandom number generators for cryptographic applications (2010).
  - [80] P. E. Kloeden and E. Platen, in *Numerical Solution of Stochastic Differential Equations* (Springer Berlin Heidelberg, Berlin, Heidelberg, 1992) pp. 103–160.
  - [81] R. J. Freund and W. J. Wilson, *Statistical Methods* (Elsevier, 2003).
  - [82] K. Pearson, The London, Edinburgh, and Dublin Philosophical Magazine and Journal of Science **50**, 157 (1900).
  - [83] D. Walls and G. Milburn, *Quantum Optics* (Springer, 2008).
  - [84] E. B. Wilson and M. M. Hilferty, Proc. Natl. Acad. Sci. U.S.A. **17**, 684 (1931).
  - [85] N. L. Johnson, *Continuous Univariate Distributions*, Houghton Mifflin Series in Statistics (Houghton Mifflin, Boston, 1970).